Direct-drive double-shell implosion: A platform for burning-plasma physics studies

S. X. Hu [1,*] R. Epstein,[1] W. Theobald,[1] H. Xu,[2] H. Huang,[2] V. N. Goncharov,[1] S. P. Regan,[1] P. W. McKenty,[1] R. Betti,[1] E. M. Campbell,[1] and D. S. Montgomery[3]

[1]*Laboratory for Laser Energetics, University of Rochester, 250 E. River Road, Rochester, New York 14623, USA*
[2]*General Atomics, San Diego, California 92121, USA*
[3]*Los Alamos National Laboratory, Los Alamos, New Mexico 87545, USA*

Double-shell ignition designs have been studied with the indirect-drive inertial confinement fusion (ICF) scheme in both simulations and experiments in which the inner-shell kinetic energy was limited to $\sim$10–15 kJ, even driven by megajoule-class lasers such as the National Ignition Facility. Since direct-drive ICF can couple more energy to the imploding shells, we have performed a detailed study on direct-drive double-shell (D^3S) implosions with state-of-the-art physics models implemented in radiation-hydrodynamic codes (LILAC and DRACO), including nonlocal thermal transport, cross-beam energy transfer (CBET), and first-principles−based material properties. To mitigate classical unstable interfaces, we have proposed the use of a tungsten-beryllium– mixed inner shell with gradient-density layers that can be made by magnetron sputtering. In our D^3S designs, a 70-μm-thick beryllium outer shell is driven symmetrically by a high-adiabat ($\alpha \geqslant 10$), 1.9-MJ laser pulse to a peak velocity of $\sim$240 km/s. Upon spherical impact, the outer shell transfers $\sim$30–40 kJ of kinetic energy to the inner shell filled with deuterium-tritium gas or liquid, giving neutron-yield energies of $\sim$6 MJ in one-dimensional simulations. Two-dimensional high-mode DRACO simulations indicated that such high-adiabat D^3S implosions are not susceptible to laser imprint, but the long-wavelength perturbations from the laser port configuration along with CBET can be detrimental to the target performance. Nevertheless, neutron yields of $\sim$0.3–1.0-MJ energies can still be obtained from our high-mode DRACO simulations. The robust α-particle bootstrap is readily reached, which could provide a viable platform for burning-plasma physics studies. Once CBET mitigation and/or more laser energy becomes available, we anticipate that break-even or moderate energy gain might be feasible with the proposed D^3S scheme.

I. INTRODUCTION

Laser-driven inertial confinement fusion [1] (ICF) has been actively pursued in the laboratory for decades. The current efforts have mainly focused on the so-called "hot-spot" ignition scheme, in which a single shell containing a solid-DT (deuterium–tritium) fuel layer covered by ablator materials is driven to implode by high-energy laser beams in either an *indirect* or *direct* way. In indirect-drive ICF, the high-energy laser beams irradiate inside a hohlraum and convert the laser energy into thermal x-ray emissions that ablatively drive the capsule (placed inside the hohlraum) to implode [2,3], while for the other scheme, the laser beams *directly* irradiate the ICF target [4,5]. For hot-spot ignition in both schemes, the single shell not only acts as the "piston" but also provides the major DT fuel for the final hot-spot formation. For the piston to have enough energy and to still be compressible at stagnation, one needs to drive the single shell for a long distance (for enough acceleration) and to maintain it at a relatively low entropy state (low adiabat). Roughly speaking, for such single-shell hot-spot ignition to work at laser energies in the MJ range, the imploding DT-containing shell must have a velocity of $V_{\text{imp}} > 350$ km/s and a high convergence ratio of $C_R > 30$ ($C_R = R_0/R_{\text{hs}}$ with R_0 being the initial shell radius and R_{hs} the final hot-spot radius). These requirements impose formidable challenges for the central-spot ignition scheme to reach the so-called *burning-plasma* stage [6], in which the self-heating of plasmas by the DT-fusion−produced α particles exceeds the radiative and conduction loss.

To reach the burning-plasma stage, the single-shell hot-spot ignition in both direct-drive and indirect-drive schemes must overcome daunting challenges, especially for the current low-margin designs due to the limited laser energy. First of all, the large C_R, low adiabat, and high implosion velocity demand stringent requirements on target and driver perturbations. For example, 3D simulations of indirect-drive ICF implosions [7] show that the driver asymmetry and target engineering features such as fill tube and interface mixing can gradually "eat" away the design margin for burning plasma to happen. The situation is also similar for direct-drive, high-convergence ICF implosions, in which the perturbations from target imperfection and long- or short-wavelength laser nonuniformities can also significantly degrade the target performance [8–11], due to the fact that these high-convergence, low-adiabat single-shell implosions are highly susceptible to violent Rayleigh-Taylor (RT) instability growth [12–17]. In addition, the DT layer being part or the whole of the piston requires tremendous effort to maintain its low entropy. Precisely timing several shocks [18–20] is necessary to set the shell in a designed

*shu@lle.rochester.edu

low adiabat. Still, excessive radiation and/or superthermal electrons produced by laser-plasma instabilities, such as two-plasmon decay [21] and stimulated Raman scattering [22], could possibly preheat the in-flight, low-temperature DT shell and render it less compressible at stagnation. All of these challenges are currently faced by the laser-drive ICF community.

Different from the above-mentioned central-spot ignition, alternative laser-fusion schemes seek to separate the hot-spot formation from the shell (piston) acceleration. Over the past two decades, some efforts in the laser-fusion community have been put into studies of these alternative schemes, including fast ignition [23,24], shock ignition [25], double-shell implosions [26–31], and a triple-shell *Revolver* design [32], just to name a few. Although these schemes have their own challenges, the separation of hot-spot formation from accelerating the piston generally relaxes the stringent requirements for the single-shell, hot-spot–ignition scheme. Taking a double-shell implosion as an example, the outer shell (piston) can be set at a much higher adiabat so that RT instability and radiation or fast-electron preheat do not significantly affect the shell integrity as it accelerates, while an inner shell composed of high-density metal layer(s) and filled with DT gas or liquid can be volumetrically shocked or compressed and heated by an $\sim$Gbar pressure reservoir that is created through the spherical stagnation (impact) of the outer shell upon the inner one. Given the electron-rich nature of a high-density inner shell, only a significantly low convergence ratio ($C_R \leqslant 10$) is needed to reach a pressure of $\sim$400 Gbar required for DT plasma burning [31]. In addition, the radiation trapping and re-emission by the high-Z inner shell can lower the ignition threshold to a relatively-low DT ion temperature ($\langle T_i \rangle \sim 3$ keV in comparison to $\langle T_i \rangle \geqslant 5$ keV in single-shell hot-spot ignition). The double-shell scheme generally trades some of the physics challenges of high-convergence ($C_R \geqslant 30$) single-shell implosions for the complexity of double-shell target fabrication and diagnoses.

For the past two decades, the study of double-shell implosions in both experiments and simulations has focused mainly on the indirect-drive scheme [26–31]. With a drive laser on the National Ignition Facility [33] (NIF) (at an $\sim$MJ energy level), recent one-dimensional (1D) simulations showed that a maximum energy of only $\sim$10–15 kJ can be coupled to the kinetic motion of the inner shell [31], even with a high-density inner-shell material like Au. The limited margin for an energetic inner shell is caused by the lower hydroefficiency in the indirect-drive scheme, in which a much thicker and massive outer shell is needed for x-ray drive. Motivated by the higher overall hydroefficiency of direct drive [5,10], we have performed a thorough investigation on whether or not a direct-drive double-shell (D^3S) platform has its own merit to create a burning plasma in the laboratory at MJ laser energy. We found that even with the currently reduced hydrocoupling caused by cross-beam energy-transfer (CBET) [34–37], direct-drive double-shell implosions can give at least twice the kinetic energy ($\sim$30 kJ) as the indirect-drive case; such a more-energetic inner shell could provide more of a margin to reach the DT-plasma burning stage, as more inner-shell kinetic energy will give more specific energy to the similar DT core in both indirect-drive and direct-drive double-shell targets. In addition, we propose to use the newly

invented technology of magnetron sputtering [38] to make a density-gradient inner shell of a tungsten-beryllium mixture. By varying the tungsten-to-beryllium concentration ratio, one may be able to construct an inner shell with density dropping from $\rho_0 \sim 19\,\text{g/cm}^3$ (97% W + 3% Be) to $\rho_0 \sim 2.2\,\text{g/cm}^3$ (1% W + 99% Be) along both inward and outward directions. The idea of using gradient-density layers, proposed earlier for single-shell ICF [16], can help to mitigate the classical RT problem during the outer-shell collision [39]. It not only reduces the Atwood number but also increases the density scale length at the collisional surface. It can be thought of as multiple "tamper" layers used for indirect-drive double-shell designs [28,29,31] but with a gradual density variation.

In the radiation-hydrodynamic studies of direct-drive double-shell implosions presented in this paper, we have used both the 1D code LILAC [40] and the 2D code DRACO [41] developed by the Laboratory for Laser Energetics (LLE) at the University of Rochester. The state-of-the-art physics models, including the nonlocal thermal-transport model [42,43], the 3D ray tracing with CBET model [34–37], accurate material properties such as first-principles equation of state (FPEOS) [44–47], first-principles opacity tables (FPOTs) [48,49], and the average-ion model [50] for the opacity and emissivity of the W-Be mixture, have been employed in our radiation-hydrodynamic simulations. The use of *first-principles*-based material properties is to accurately account for target compressibility and radiation transports under extreme conditions. With a very high adiabat laser pulse of 1.9 MJ energy illuminating symmetrically on a designed double-shell capsule, we can obtain a neutron yield of $\sim$6 MJ in 1D simulations. High-mode 2D DRACO simulations with OMEGA laser port geometry and 2D smoothing by spectral dispersion (SSD) show that even though short-wavelength laser imprint is not a concern, long-wavelength beam-port perturbations on the outer shell can transfer to the inner shell, which could quench down the DT burn; nevertheless, robust burning plasmas with up to $\sim$MJ neutron yields can still result from such direct-drive double-shell implosions.

This paper is organized as follows: A brief design consideration is given in Sec. II, followed in Sec. III by the detailed 1D simulation and explanation of the dynamics of a direct-drive double-shell implosion. In Sec. IV, we present the high-mode 2D DRACO simulation results of the designed D^3S target, including laser imprint and long-wavelength laser perturbations. We also analyze the different mode growths for both outer and inner shells during the entire implosion process. The implosion performance's dependence on the density of cushion CH foam is also examined in this section. Finally, we summarize our findings in Sec. V.

II. DESIGN CONSIDERATION FOR DIRECT-DRIVE DOUBLE-SHELL IMPLOSIONS

We start with an estimated pressure of $\sim$400 Gbar and a minimum compression of $\rho R \approx 300\,\text{mg/cm}^2$, in which the α-particle heating becomes dominant over radiation and heat-conduction losses. These conditions are required for a burning DT plasma; with that we can work backward to roughly determine the target parameters. Simply assuming an ideal-gas equation of state (EOS) ($P = nkT$) for the hot

and dense DT plasma, the $\sim$400-Gbar pressure approximately means a required DT density of $\rho_{DT} \approx 100\,\mathrm{g/cm^3}$ and $kT \approx 5\,\mathrm{keV}$. At this density, the minimum $\rho R \approx 300\,\mathrm{mg/cm^2}$ for α-particle heating requires a radius of $R_{hs} = 30\,\mu\mathrm{m}$ for the spherically compressed DT fuel. Let us assume the inner shell is made of pure tungsten (W) with an initial density of $\rho_0 \approx 19\,\mathrm{g/cm^3}$ and at stagnation the tungsten pressure is equal to the $\sim$400-Gbar DT pressure (isobaric condition). To estimate the required tungsten density at stagnation, we use the electronic Fermi-degeneracy pressure (the condition of $T \ll T_F$ is always satisfied for inner shells made of heavy metals like W and Au):

$$P_F = \frac{(3\pi^2)^{2/3}\hbar^2}{5m_e}\left(\frac{\langle Z\rangle\rho_W}{A_W}\right)^{5/3}, \tag{1}$$

with electron mass m_e, the ionization degree $\langle Z\rangle$, and atomic mass $A_W = 183.84$ amu for W. This estimation gives $\rho_W \sim 1500$–$3000\,\mathrm{g/cm^3}$ depending on ionization for a final pressure of $P_F \geqslant 400$ Gbar. For example, to reach a final density of $\rho_W \approx 2000\,\mathrm{g/cm^3}$, the initial tungsten layer needs only a small convergence ratio of $C_W \sim R_i/R_f \sim 5$ to 7 depending on the layer thickness! But for DT fuel to reach its final density of $\rho_{DT} \approx 100\,\mathrm{g/cm^3}$ from initial liquid ($\rho_i \approx 0.2\,\mathrm{g/cm^3}$), one needs a convergence ratio to be $C_{DT} = (\rho_{DT}/\rho_i)^{1/3} \sim 8$. Reconciling for both DT and W layers, a choice of convergence ratio of $C_R \geqslant 8$ should be good enough. Therefore, given the final radius of $R_{hs} = 30\,\mu\mathrm{m}$ for the compressed DT sphere, the design requires the initial inner-shell radius to be $R_{inner} \geqslant 240\,\mu\mathrm{m}$ if filled with liquid DT.

Now we estimate the internal energies in the stagnated DT + W system. Given the above parameters, the compressed and heated DT sphere will have an internal energy of $E_{DT} = 3NkT \approx 7.4\,\mathrm{kJ}$ (N being the total number of DT particles). For an $\sim$30-μm-thick initial tungsten layer (similar to what is used in *indirect-drive* double-shell designs and roughly corresponding to the final DT-core size) starting at $R_{i1} = 240\,\mu\mathrm{m}$ and ending at $R_{i2} = 270\,\mu\mathrm{m}$, we determine the final inner and outer radii for the compressed W layer to be $R_{f1} = 30\,\mu\mathrm{m}$ and $R_{f2} = 43.6\,\mu\mathrm{m}$, respectively, to reach a density of $\rho_W \sim 2000\,\mathrm{g/cm^3}$. The compression costs energy that can be roughly estimated as the rising Fermi energy per electron multiplied by the total number of free electrons in the final compressed W shell ($\langle Z\rangle \sim 38$ estimated from the average-atom model). Namely, we arrive at

$$E_W = \hbar^2(3\pi^2\rho_W\langle Z\rangle/A_W)^{2/3}/2m_e \times \langle Z\rangle \times \rho_W/A_W$$
$$\times 4\pi(R_{f2}^3 - R_{f1}^3)/3 \simeq 13.4\,\mathrm{kJ}$$

(neglecting its small initial internal energy). Therefore, the total energy needed to assemble the final burning-plasma target is about $E_{tot} \approx 20.8\,\mathrm{kJ}$ (7.4 kJ for DT and 13.4 kJ needed for W compression), which is provided by the kinetic energy of the imploding inner shell. This gives an estimated implosion velocity of $V_{inner} = \sqrt{2E_{tot}/M_{inner}} \simeq 298\mathrm{km/s}$, for the assumed 30-$\mu$m-thick pure tungsten inner shell. If the inner-shell thickness is increased, the implosion velocity can be further lowered to a comfortable range of $V_{inner} = 220$–$250\,\mathrm{km/s}$ (discussed below).

Upon the spherical collision of the outer shell, an $\sim$Gbar pressure reservoir is created in the compressed and heated

CH-foam cushion layer that was originally placed between the two shells. Depending on the total mass of the CH-foam layer, this spherical collision could vary from completely inelastic to elastic [31]. Assuming conservatively that only one-third of the outer-shell kinetic energy transfers to the inner shell, two-thirds are used to create the pressure reservoir and to compress the outer shell at collision. This simply means that the imploding outer shell should have a kinetic energy of $K_{outer} = 3 \times 20.8 = 62.4\,\mathrm{kJ}$. With respect to a NIF-scale drive laser energy of $E_L = 1.9\,\mathrm{MJ}$, it means a hydrocoupling efficiency of $\geqslant 3.5\%$ should give the required outer-shell kinetic energy. In comparison with the studied *indirect-drive* scheme, the *direct-drive* method will give more of a margin for double-shell designs. Even with the currently unavoidable influence of CBET, a hydrocoupling efficiency above $\sim 4\%$ had been demonstrated by direct-drive implosions for ablator materials ranging from CH to Be (Ref. [51]). Here, we choose pure beryllium as the outer-shell material because of its superior thermal conductivity scaling as A/Z (leading to higher ablation velocity and hydroefficiency). Giving the hydroefficiency of $\eta \sim 4\%$, a NIF-scale laser of $E_L = 1.9\,\mathrm{MJ}$ could symmetrically drive the $\sim$70-μm-thick outer Be shell (starting at $R_{o2} \sim 1500\,\mu\mathrm{m}$ and ending at $R_{o1} \sim 1570\,\mu\mathrm{m}$) to an implosion velocity of $V_{outer} \approx 240\,\mathrm{km/s}$. This should provide enough kinetic energy to drive the required inner-shell implosion for assembling a burning DT plasma. Again, the lower implosion velocity is one of the advantages for D^3S implosions rather than single-shell hot-spot ignition. The choice of 70-μm-thick Be outer shell is from a balanced consideration that a thinner Be layer is good for getting higher hydro-efficiency, but it would be susceptible to disruption of the RT instability. The chosen outer-shell radius is resulted from the consideration of the overlap laser intensity on target ($<10^{15}\,\mathrm{W/cm^2}$) and the total laser peak power.

Giving more margins than the above 1D considerations, we end up with the double-shell target design shown in Fig. 1. It
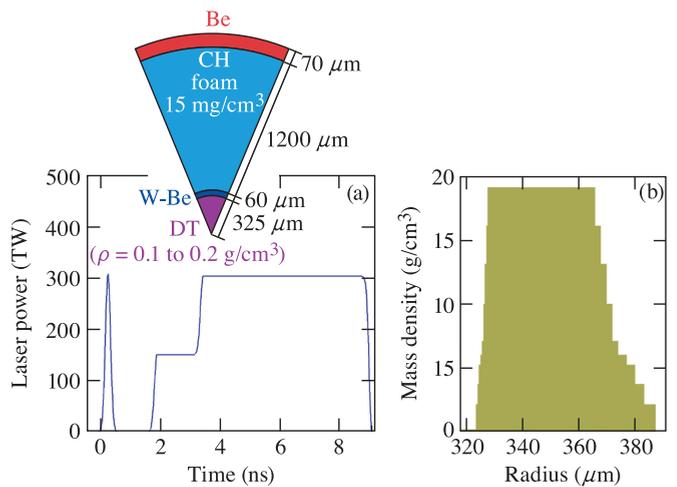
FIG. 1. (a) The high-adiabat laser pulse shape and target dimensions for the proposed direct-drive double-shell implosion, of which the inner shell is made of a tungsten-beryllium mixture with density gradient; (b) the inner-shell density profile as a function of target radius in which the W-Be-mixture layers of different compositions give varying densities in both outward and inward directions.

TABLE I. The composition and mass for each part of a typical direct-drive double-shell target design.

	Materials	$\rho(\text{g/cm}^3)$	$R_{\text{start}}(\mu\text{m})$	$R_{\text{end}}(\mu\text{m})$	Mass (mg)
Core	DT (liquid)	0.20	0	325	0.029
Inner shell	W-Be mixture	2.2 to 19.0	325	385	1.30
Mid fill	CH foam	0.015	385	1585	0.33
Outer shell	Be	1.84	1585	1655	4.25

consists of an $\sim$60-μm-thick tungsten-beryllium–mixed inner shell (starting at $R_{i1} \sim 325\,\mu$m and ending at $R_{i2} \sim 385\,\mu$m), which has a density distribution illustrated by Fig. 1(b). The constant high-density portion of $\rho_{\text{BeW}} \sim 19\,\text{g/cm}^3$, having a thickness of $\sim$35 μm, is made of a mixture of 97% W and 3% Be. The outward portion of $\sim$21 μm has eight layers with densities varying from $\rho_{\text{BeW}} \sim 16\,\text{g/cm}^3$ down to $\rho_{\text{BeW}} \sim 2.2\,\text{g/cm}^3$ for the outermost layer (1% W + 99% Be). Similarly, there are also 4-μm gradient-density layers inward of the constant high-density portion. As discussed above, these gradient-density layers help to mitigate the classical RT issue during both acceleration and deceleration phases of the imploding inner shell. The inner shell will be filled with either DT liquid or DT gas with a density of $\rho_{\text{DT}} \approx 0.1$–$0.2\,\text{g/cm}^3$. The pure-Be outer shell has a thickness of $\sim$70 μm and an initial density of $\rho_{\text{Be}} \approx 1.84\,\text{g/cm}^3$. This optimal choice of Be outer-shell thickness is from considerations of both RT instability and the fact that a relatively massive shell can maintain a longer pressure pulse for the inner shell to accelerate. The cushion layer between the two shells is filled with CH foam of $\rho_{\text{CH foam}} \sim 10$–$20\,\text{mg/cm}^3$. The outer radius of the overall target is equal to $r = 1.655\,\text{mm}$. The composition and mass for each part of this typical direct-shell double-shell target are listed in Table I. The double-shell target is designed for implosion by a symmetric direct-drive laser pulse shown in Fig. 1(a) ($E_\text{L} = 1.9\,\text{MJ}$). The high-intensity picket sets up the outer shell to a very high entropy state (high adiabat α defined as $\alpha = P/P_F$, which is the ratio of in-flight shell pressure to its degenerated Fermi pressure). It is noted that shock timing is not needed for such double-shell targets. To have a high-adiabat outer-shell implosion, we intentionally allow the first strong shock to break out early, and the second shock transits through the decompressed Be plasma to create an unusually high adiabat ($\alpha \geqslant 10$) shell to avoid the imprint-seeded RT instability concern. Whether or not the high-entropy outer shell is insensitive to any potential preheat from radiation and laser-plasma instability (LPI)–produced fast electrons remains to be explored.

III. ONE-DIMENSIONAL DYNAMICS OF DIRECT-DRIVE DOUBLE-SHELL IMPLOSIONS

We begin our discussion with the 1D dynamics of direct-drive double-shell implosions. Using LLE's 1D radiation-hydrodynamic code LILAC [40], we simulate the implosion of a double-shell target directly driven by a NIF-scale laser pulse ($E_\text{L} = 1.9\,\text{MJ}$) with a peak laser intensity of $\sim$8 $\times$ $10^{14}\,\text{W/cm}^2$, both of which are shown in Fig. 1. In the simulation, we have employed state-of-the-art models including the nonlocal thermal transport model of iSNB [42,43],

the CBET model [34–37], and accurate material properties such as FPEOS [44–47] and FPOT [48,49]. The opacity and emissivity modeling of the W-Be mixture was based on the average-ion model calculated in the collisional-radiative limit [50], while the astrophysical opacity table was used for the Be outer shell. The implosion dynamics are illustrated in Fig. 2, where the Lagrangian layer position is plotted as a function of implosion time. We see that the high-intensity laser picket first launches a very strong shock into the outer Be shell, which breaks out from the back surface at $t \approx 1.4$ ns. Next, the shocked outer shell starts to decompress and move inward. The second and third shocks launched by the step- or main-pulse transit through the decompressed and already moved Be shell during 2 to 4 ns. When they break out and the rarefaction wave reaches the ablation front at $t = 5$ ns, the strong acceleration of the outer shell (blue) begins and pushes the CH-foam layer (gray) inward. Meanwhile, we see the gradient-density W-Be layer (green, the outer portion of the inner shell) expand as a result of radiation preheating. At the end of the laser pulse ($t = 9$ ns), the outer Be shell stagnates on the inner shell, with the CH-foam cushion layer stuck in between. A pressure reservoir of $P > 2$ Gbar is created, launching a very strong shock into the inner shell and the DT fuel. Subsequently, the pressure reservoir drives the inner shell to implode. At around $t = 11$ ns, the inner shell stagnates, converting its kinetic energy to both DT-fuel heating and
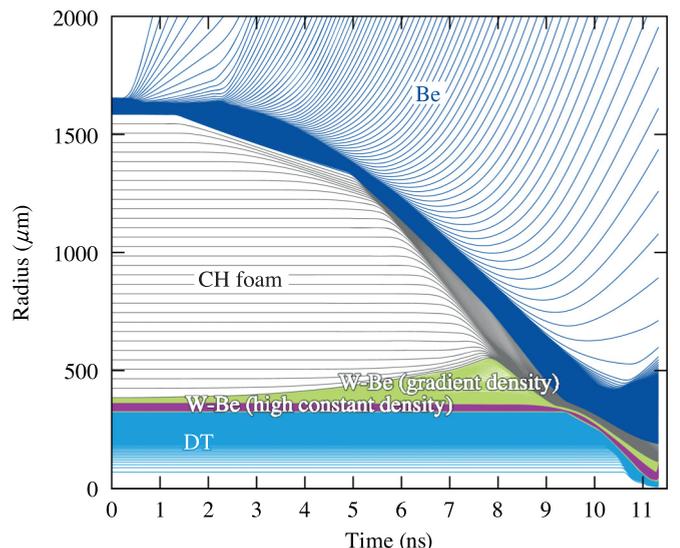
FIG. 2. The Lagrangian layer position as a function of time that shows the entire dynamics of a direct-drive double-shell implosion.
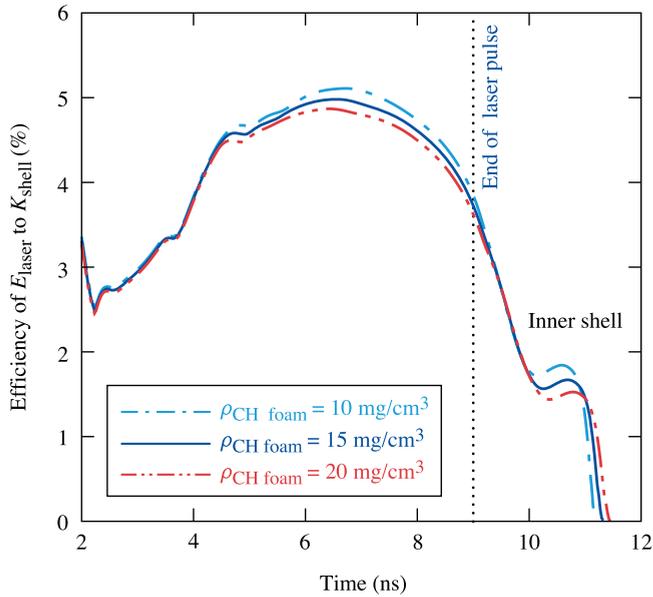
FIG. 3. The drive efficiency from laser energy to the kinetic energy of the imploding shells, predicted by 1D hydrocode LILAC, is plotted as a function of time.

FIG. 4. The LILAC-predicted profiles of density, temperature, adibat, and velocity as functions of target radius for different times: (a), (b) the imploding outer shell at $t = 5.4$ ns and $t = 7.0$ ns, respectively; (c) the outer shell colliding on the inner shell at $t = 8.8$ ns; and (d) the imploding inner shell at $t = 10.9$ ns.

inner-shell compression. At the end, the compressed DT fuel is volumetrically ignited.

To investigate the energetics of direct-drive double-shell implosions, we plot in Fig. 3 the coupling efficiency of laser energy to the kinetic energy of both outer and inner shells. The time-dependent coupling efficiency is defined as $\eta(t) = (1/2)M_{shell}(t)V(t)^2 / \int_0^t E_L(t')dt'$, where the mass and velocity are taken only for the portion of shell moving inward. In these simulations, we have considered three different CH-foam densities of $\rho_{CH\,foam} = 10$, 15, and 20 mg/cm^3 for the cushion layer. For all three cases, the laser absorption fraction is on the level of ~70% under full CBET. Figure 3 indicates that at the end of the laser pulse (marked by the vertical dotted line) there is ~3.6% laser energy coupled to the outer shell, even with the full CBET effect taken into account. It is noted that wavelength detuning with $\Delta\lambda_{UV} = 3$ to 6 Å could partially reduce the CBET effect so that a higher hydroefficiency can be expected for the current D^3S design, which is a topic for future optimization. After the collision, half of the outer-shell kinetic energy is converted to the inner-shell motion. Namely, the final kinetic energy of the inner shell is about 28.5–34.2 kJ (i.e., ~1.5–1.8% of 1.9-MJ laser energy), depending on the CH foam density. This efficiency is lower than single-shell hot-spot ignition in direct-drive targets, but is roughly on the same level of indirect-drive ICF targets. As can be seen from Fig. 3, the use of lower-density CH foam favors slightly more energy transfer (more elastic collision and less energy wasted in the cushion layer). However, a higher foam density can help to efficiently "filter" out perturbations of the outer shell so that less perturbation feeds into the inner shell. A balance between the two choices leads to an optimal CH-foam density of $\rho_{CH\,foam} = 15$ mg/cm^3 for the best target performance, which will be studied in detail in the following section.

In Fig. 4, we plot the LILAC-predicted profiles of density, temperature, adiabat, and velocity as functions of target radius

for several snapshots during the implosion. Figure 4(a) shows the early stage of the implosion when the outer Be shell starts to accelerate at $t = 5.4$ ns. Due to the very high laser intensity of the picket, the Be shell is heated to a high temperature of $kT \approx 40$ eV (dashed light-blue line) and the peak density is only about twice the solid density of Be. As the implosion proceeds, the in-flight Be shell is assembled into a very high adiabat ($\alpha \geqslant 10$) state, as illustrated by the dashed blue line in Fig. 4(b). It can be seen that the in-flight aspect ratio (IFAR) is only about ~20 (conventionally defined as IFAR $= R/\delta R$ at the shell converging to two-thirds of its original radius), which is significantly lower than the usual single-shell low-adiabat ignition designs of IFAR $\geqslant 30$. The high adiabat and reduced IFAR should make such direct-drive double-shell implosions less susceptible to RT instabilities. Figure 4(c) illustrates the situation near the end of outer-shell acceleration ($t = 8.8$ ns), in which the outer shell (at $R \sim 600\,\mu$m) has an average velocity of $V_{imp} \approx 240$ km/s and impacts onto the inner shell. A small shock is also seen at $R \approx 400\,\mu$m propagating toward the inner shell that has been precompressed as a result of the radiation-induced expansion of its outer layer. Finally, Fig. 4(d) shows the inner-shell implosion (at $t = 10.9$ ns) after collision. A high-density inner shell of $\rho > 200$ g/cm^3 is imploded with a modest velocity of $V_{imp} \approx 230$ km/s. The shock that has bounced back in the liquid DT is also evidenced at this time, i.e., a high-DT-density "bump" is observed at around $R \sim 60\,\mu$m. This is due to the fact that when the outgoing DT shock encounters the inner shell of higher pressure, it reflects back into the DT. As the deceleration of the inner shell begins, the shock in the DT bounces back and forth between the origin and the imploding high-pressure inner shell. This behavior manifests itself when we look at the averaged velocity of
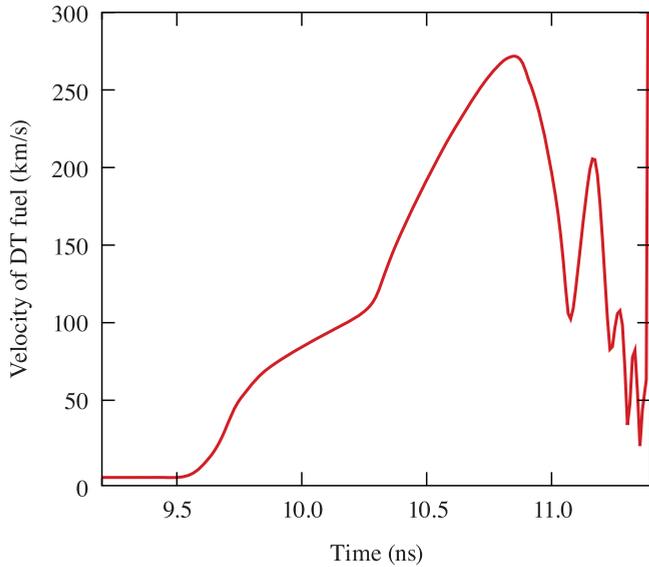
FIG. 5. The LILAC-predicted averaged-velocity evolution of DT fuel that is shocked and consequently pushed inward by the dense inner shell. The several oscillations before stagnation indicate the complicated dynamics of the shock bouncing back and forth between the spherical origin and the imploding high-pressure inner shell.

FIG. 6. Density contour plots on the r,z plane from 2D DRACO simulations of the direct-drive double-shell implosion during the outer-shell acceleration phase at different times of (a) $t = 4.0$ ns, (b) $t = 5.5$ ns, (c) $t = 7.0$ ns, and (d) $t = 9.0$ ns.

DT fuel during the implosion in Fig. 5. One sees that at $t = 10.9$ ns the velocity of DT fuel reaches its maximum due to the compression by the inner shell; after that the DT-fuel velocity decreases as its kinetic energy converts into thermal energy (heating). Several such velocity oscillations are observed during this kinetic-to-thermal energy conversion, as shocks bounce back and forth in the DT fuel. It is noted that the initial DT-velocity increase at $t \approx 9.7$ ns is caused by the strong shock originating from the outer- to inner-shell collision. Finally, most of the kinetic energy converts into the pressure of the DT fuel at around $t \approx 11.3$ ns, when the ignition occurs. It is noted that the strong shock convergence indeed creates a "hot spot" in the liquid DT fuel. However, this shock-created hot spot is not dense and hot enough to initiate the burn. Instead, the subsequent compression and heat bring the DT-fuel to *volumetric* ignition. The 1D target performance is summarized in Table II for the optimal CH-foam density, in which a neutron yield of $Y \approx 2.1 \times 10^{18}$ (a factor of $\sim$100 for α amplification) can be reached (corresponding to an output energy of $\sim$6 MJ and a gain of $G \sim 3$). The pre-burn $\langle kT_{no-\alpha} \rangle = 2.9$ keV is significantly lower than the hot-spot ignition.

TABLE II. Summary of 1D target performance for the direct-drive double-shell implosion design.

Target performance	CH foam (15 mg/cm^3)
Neutron yield	2.1×10^{18}
$\langle \rho R \rangle_{DT}$	605 mg/cm^2
$\langle \rho R \rangle_{shell}$	3.8 g/cm^2
$\langle T_i \rangle$	30.8 keV
$\langle P \rangle$	4.5 Tbar

IV. TWO-DIMENSIONAL DRACO SIMULATIONS

In this section, we perform 2D DRACO simulations for the direct-drive double-shell target designs discussed above, using its Lagrangian version with rezoning. Again, we will focus on the D^3S target with an optimized CH-foam density of 15 mg/cm^3, even though the other two situations of $\rho_{CH foam} = 10$ mg/cm^3 and $\rho_{CH foam} = 20$ mg/cm^3 are also simulated. These high-mode DRACO simulations, with a grid size of 605×450 respectively for radial and angular dimensions, have included both long-wavelength port-geometry perturbation and short-wavelength laser imprint up to a maximum mode of $\ell_{max} = 150$ since laser nonuniformity is always a concern for direct-drive ICF. Laser imprinting is simulated in DRACO by decomposing the distributed phase plate (DPP) spectra into individual modes that perturb the spatial distribution of laser ray energies accordingly [37,52]. Again, we are considering the OMEGA beam geometry and beam conditions of polarization smoothing plus 2D SSD; the CBET and nonlocal thermal transport models are applied in these DRACO simulations, in which the first-principles material properties are also invoked. When compared to no-CBET cases, the energy loss is about $\sim$20% reduction in laser energy absorption; and the laser-port perturbation is enhanced by CBET. The radiation hydrocode DRACO uses the cylindrical symmetry where z is the symmetry axis and r is the radial axis. As an example, we have shown the density contour plots on the r, z plane in Fig. 6 while the outer shell is imploding, respectively, at times of (a) $t = 4.0$ ns, (b) $t = 5.5$ ns, (c) $t = 7.0$ ns, and (d) $t = 9.0$ ns. At the end of the laser pulse ($t = 9.0$ ns), the outer shell has a convergence ratio of only $C_R \sim 3$! One sees that as the implosion proceeds, the density perturbations at the ablation front (induced by laser nonuniformity) are growing
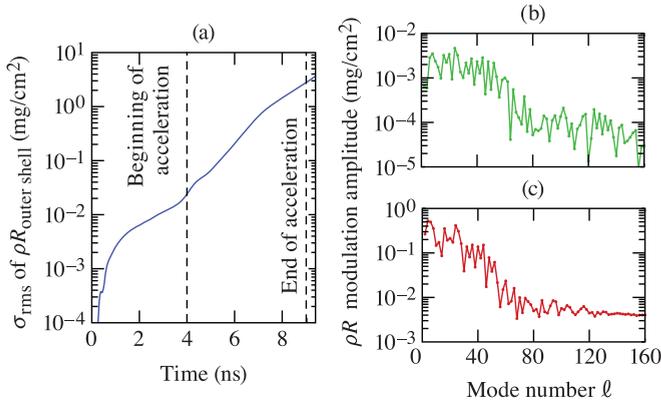
FIG. 7. (a) The root mean square (σ_{rms}) of areal-density (ρR) modulation of the imploding outer shell as a function of time. The modal spectra of $\rho R_{outer\,shell}$ modulation at (b) the beginning of acceleration ($t = 4.0$ ns) and (c) at the end of the acceleration phase ($t = 9.0$ ns).

FIG. 8. The density and pressure contour plots on the r,z plane: (a), (b) as the outer shell impacts on the inner shell at $t = 10.0$ ns; (c), (d) as the inner shell accelerates inward after the collision ($t = 10.5$ ns). (b) and (d) indicate that a pressure over ~ 2 Gbar is created and maintained for ~ 1 ns.

because of the RT instability. Because of the high adiabat ($\alpha \geqslant 10$) of the outer Be shell, however, the perturbation growth is insignificant so that the outer-shell integrity is still good [Fig. 6(d)]. Namely, the density perturbation does not penetrate through the entire shell, which is essential to having acceptable target performance. To quantify the RT growth, we have plotted the ρR perturbation (σ_{rms}) of the outer shell as a function of time in Fig. 7(a). The shell acceleration starts at $t \sim 4$ ns and ends at $t \sim 9$ ns, during which the ρR perturbation grows from $\sigma_{rms} \approx 0.02$ mg/cm^2 to $\sigma_{rms} \approx 2.5$ mg/cm^2 (i.e., by a factor of ~ 125). This is significantly lower than low-adiabat single-shell implosions where the growth factor is on the level of 500–1000 for the CH ablator [11]. In Figs. 7(b) and 7(c), the modal spectra of ρR perturbation are shown, respectively, for the beginning and the end of outer-shell acceleration. One sees that the higher modes ($\ell > 80$) grow by only a factor of ~ 20, while the amplitudes of low or mid modes ($\ell = 2$–60) increase by a factor of 100–150 after the entire acceleration phase. This clearly indicates this design is insusceptible to laser imprint. Overall, the RT instability growth is relatively low and the outer-shell integrity is still good at the end of the laser pulse.

After the end of the laser pulse, the outer Be shell is in a so-called "coasting" phase for ~ 1 ns. Once it collides with the inner shell at $t = 10$ ns, it creates a pressure reservoir of $P > 2$ Gbar as shown by Figs. 8(a) and 8(b). During this collision process, the outer Be shell slows down and transfers its kinetic energy to heat the CH-foam cushion layer, thereby creating the high-pressure reservoir. This stagnation process also compresses the outer Be shell. Subsequently, a very strong shock is launched into the inner shell; when the shock breaks out, the inner shell becomes significantly accelerated inward, which is illustrated for the situation at $t = 10.5$ ns by Fig. 8(c). Figure 8(d) shows that at this time the reservoir still remains at a high pressure of $P > 2$ Gbar. This is partially due to the fact that the outer Be shell is still comoving inward with the inner shell. Namely, the outer Be shell was significantly slowed down but not completely stopped, which helped to maintain the pressure reservoir for sufficiently long
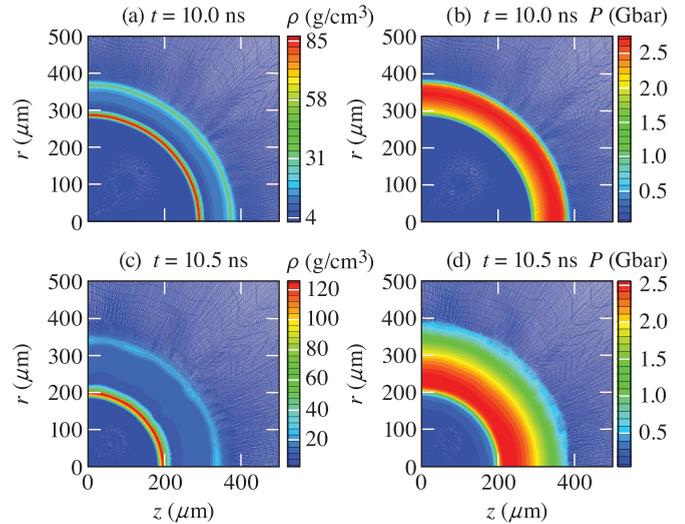
acceleration of the inner shell (~ 1 ns). Another interesting fact that can be seen in Fig. 8(c) is that some long-wavelength perturbations are transferred from the outer shell onto the inner shell. The foam layer, being compressed to a thickness of $\sim 100\ \mu$m (in between the two shells), acts like a filter to damp any perturbations having wavelength shorter than the squeezed foam-layer thickness. We quantify this perturbation transfer in Fig. 9 for these two snapshots during the collision. Figure 9(a) shows the ρR modulation spectrum of the outer shell at $t = 10.0$ ns, in which we again see that only low or
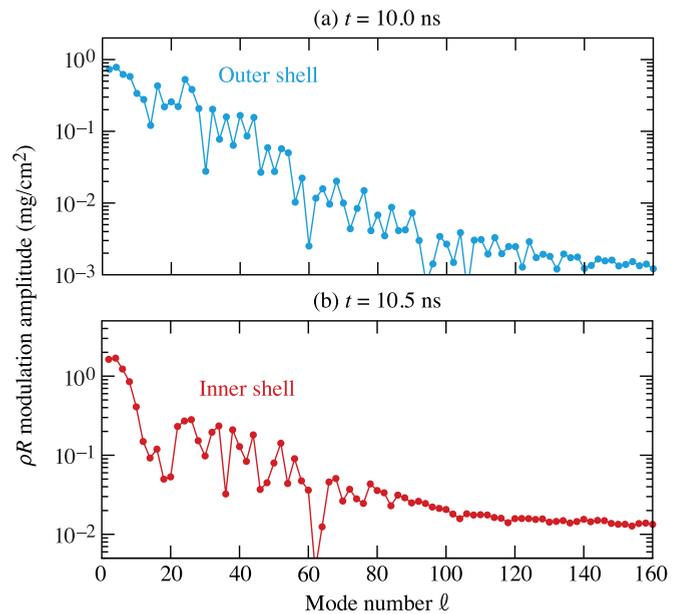
FIG. 9. The modal spectra of ρR modulations for (a) the outer shell at $t = 10.0$ ns (during collision) and (b) the inner shell at $t = 10.5$ ns after the collision.
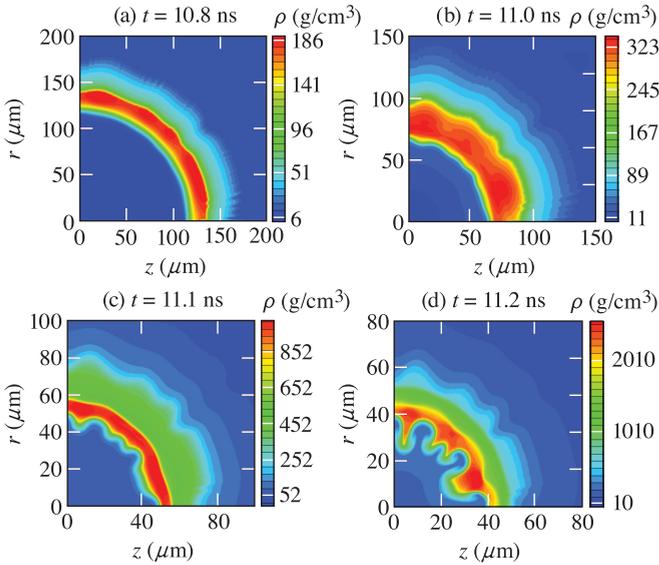
FIG. 10. The density contour plots on the r,z plane during the inner-shell implosion at different times: (a) $t = 10.8$ ns, (b) $t = 11.0$ ns, (c) $t = 11.1$ ns, and (d) $t = 11.2$ ns. The first two snapshots correspond to the acceleration phase of the imploding inner shell, while the latter two snapshots correspond to the deceleration phase.

FIG. 11. (a) The root mean square (σ_{rms}) of ρR modulation of the imploding inner shell as a function of time. (b) The modal spectral evolution from $t = 10.5$ ns to $t = 11.2$ ns for the beginning of acceleration and the end of deceleration of the inner shell, respectively.

mid modes of $\ell < 60$ are significant ($> 0.05 \, \text{mg/cm}^2$). After the collision, these modes "imprint" on the inner shell as indicated by Fig. 9(b) in which only these modes have significant amplitude of $\rho R > 0.1 \, \text{mg/cm}^2$. They are the seeds for the subsequent RT-instability growth during the inner-shell acceleration.

Figure 10 illustrates both acceleration and deceleration phases of the inner shell during its implosion. Again, we plot the density contours in the r,z plane for different times of (a) $t = 10.8$ ns, (b) $t = 11.0$ ns, (c) $t = 11.1$ ns, and (d) $t = 11.2$ ns. Figures 10(a) and 10(b) show that the very long wavelength perturbations ($\ell \leqslant 20$) caused by port geometry are growing significantly in the inner-shell density contours. These long-wavelength modes, coming from port geometry and being enhanced by CBET, feed through the inner-shell thickness so that the inner surface becomes modulated at the end of acceleration [see Fig. 10(b)]. This modulated inner surface will become unstable during the inner-shell deceleration. As Figs. 10(c) and 10(d) illustrate, they grow exponentially during the deceleration phase. We further quantitatively examine these RT growths in Fig. 11 by plotting the σ_{rms} of the inner-shell ρR as a function of time in Fig. 11(a). We see that starting at $t \approx 10.4$ ns, the inner-shell ρR perturbation grows from $\sigma_{rms} = 0.004 \, \text{g/cm}^2$ to $\sigma_{rms} \approx 0.1 \, \text{g/cm}^2$ at $t = 11.1$ ns. Immediately after that, the growth slope becomes steeper and lasts ~ 200 ps, manifesting the violent growth in the deceleration phase. In Fig. 11(b), we plot the time history of ρR modulation spectra for the dominant long-wavelength modes. We observe that the mid modes of $\ell = 20$ to 60 grow by only a factor of ~ 20 (from 1–$3 \times 10^{-4} \, \text{g/cm}^2$ to 2–$6 \times 10^{-3} \, \text{g/cm}^2$), while the low-mode ($\ell \leqslant 20$) amplitudes are increased by a factor of ~ 100. At $t = 11.2$ ns, the low-mode perturbations have grown into large spikes shown by Fig. 10(d). These low-wavelength spikes (originally caused by
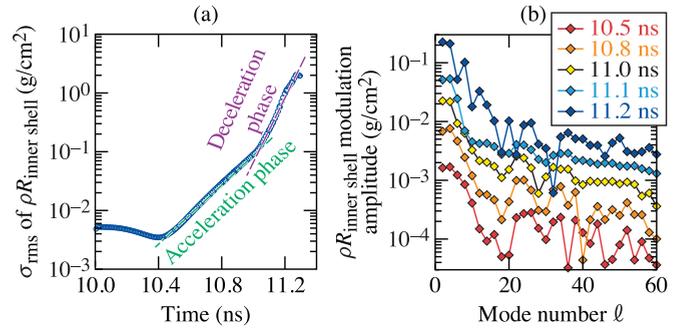
beam overlapping from different laser ports) penetrating into the DT fuel degrade the target performance in the following two ways: (1) reducing the clean volume by a factor of ~ 3 and decreasing the burning-plasma temperature by a factor of ~ 2; and (2) preventing the complete conversion of inner-shell kinetic energy into thermal heating of the DT fuel. We found that to reach numerical convergence for such nonlinear RT growth, one needs a very fine grid, even for such long-wavelength perturbations. It is noted that compensating these long-wavelength perturbations by target shimming (varying shell thickness by imposing certain modes) might be possible.

Finally, we show the last stage of the direct-drive double-shell implosion in Fig. 12, i.e., the burning of the DT plasma. Despite the significant long-wavelength perturbation growth during the deceleration phase, the DT fuel has been compressed and heated to a density that is hot enough for the burn to begin. Figure 12(a) indicates the starting point of the plasma burning, in which the upper and lower panels give the density and ion temperature contours, respectively. It shows that the stagnation has compressed the inner shell to $\rho \sim 2500 \, \text{g/cm}^3$ and the DT fuel to $\rho \geqslant 200 \, \text{g/cm}^3$, and the ion temperature is approaching $T_i > 5 \, \text{keV}$. From this instant on, the bootstrap heating begins rapidly so the ion temperature keeps increasing because of the self-heating caused by the fusion-produced α particles becoming larger than the total loss as a result of radiation and thermal conduction. It is noted that the dense, high-Z inner shell helps to reduce the two loss mechanisms because (1) the radiation lost to the high-Z shell can partially re-emit back to the DT fuel and (2) the thermal conductivity generally scales as $\kappa \propto 1/Z$. Once the DT plasma starts to burn, the ion temperature increases quickly. After 40 ps of DT burning, the peak ion temperature reaches $kT_i > 16 \, \text{keV}$ as shown in Fig. 12(b). The burning DT creates an extremely high pressure of over ~ 1000 Gbar that launches the final strong shock propagating into the already compressed inner shell and pushes its density to $\rho_{\text{inner shell}} > 3000 \, \text{g/cm}^3$. This burning plasma is inertially confined for ~ 150 ps by the inner shell because of its high $\rho R (> 3.5 \, \text{g/cm}^2)$. At the end, the DRACO simulation gives a neutron yield of $Y = 3.56 \times 10^{17}$ (~ 1 MJ energy corresponding to a gain of $G \sim 0.53$). The dynamics of volumetric burning is the same as what was described in the literature [31,32,53].

FIG. 12. The density (ρ) and ion temperature (T_i) contour plots on the r, z plane during the inner-shell stagnation: (a) at the beginning of bootstrap heating ($t = 11.23$ ns) and (b) at the peak neutron production ($t = 11.27$ ns) when the burning-plasma stage is reached.

In comparison to the 1D result, our 2D simulations showed that the long-wavelength perturbation growth can reduce the target gain by a factor of ~ 6. For these dominant long-wavelength perturbations, previous works indicated that 2D simulations should give proper account for their 3D behaviors, although 3D short-wavelength ($\ell \geqslant 100$) growth might be significantly different from 2D predictions. Even if 3D simulations and experiments can further degrade our 2D results by an additional factor of 2–4, we still expect a neutron yield of ~ 250–500 kJ from such D^3S implosions. It can still provide a viable platform for burning-plasma studies in laboratories.

In addition, we have varied these designs by changing the inner- or outer-shell thickness, the target size, the DT density from liquid to gas, and the density of the CH-foam cushion layer. A total of ten high-mode DRACO simulations were performed for these designs, with all reaching the burning-plasma stage and giving neutron yields ranging from $\sim 1.0 \times 10^{17}$–3.6×10^{17} (corresponding to total neutron energies of $E_{output} \approx 300$–1000 kJ). As an example, Table III summarizes the high-mode DRACO simulation results for three direct-drive double-shell designs similar to the design discussed above, but with three different CH-foam densities. Although the low-density foam layer gives more kinetic energy transferred to the inner shell (see Fig. 3), more perturbation growth quenches down the plasma burning more significantly than the other two situations. Nevertheless, all three give burning DT plasmas

TABLE III. Summary of 2D DRACO simulation results for similar direct-drive double-shell implosion designs but with different CH-foam densities.

Target Performance	CH foam (10 mg/cm^3)	CH foam (15 mg/cm^3)	CH foam (20 mg/cm^3)
Neutron yield	1.18×10^{17}	3.56×10^{17}	2.47×10^{17}
Neutron yield energy	330 kJ	1005 kJ	697 kJ
$\langle \rho R \rangle_{DT}$	584 mg/cm^2	524 mg/cm^2	522 mg/cm^2
$\langle T_i \rangle$	6.9 keV	9.8 keV	8.3 keV

with output energies of $E_{output} > 300$ kJ. Note that each of the high-mode DRACO simulations took about two months to complete on our Lenovo cluster ("Typhoon") running with 360 cores. It is also noted that a warm D^3S target filled with DT gas of $\rho_i = 0.1$ g/cm^3 can also give ~ 1-MJ neutron yield. Even though these direct-drive double-shell designs do not reach the break-even point under the current constraints of CBET and limited laser energy, they might provide a robust platform for studying burning-plasma physics.

V. SUMMARY

Considering the larger laser-to-target coupling efficiency of direct-drive ICF, we have performed a detailed design study of (D^3S) implosions, using both 1D and 2D radiation-hydrodynamic simulations. The design simulations have used state-of-the-art physics models including nonlocal thermal transport, 3D ray tracing with CBET, and first-principles–based material properties. In our symmetrical D^3S designs, we have employed the NIF-scale laser energy of ~ 1.9 MJ with an OMEGA-type beam geometry. A simple laser pulse with a very high intensity picket is applied to set the outer shell on an extremely high adiabat ($\alpha \geqslant 10$) so that it is not susceptible to laser imprint and preheat. The target consists of a 70-μm-thick beryllium outer shell and a 60-μm-thick inner shell of a tungsten-beryllium (W-Be) mixture, with a low-density CH-foam layer (1200 μm) between the two shells. The inner core can be filled with either DT gas or liquid DT fuel. To mitigate the classical RT instability, gradient-density W-Be–mixed layers are used as multiple "tamper" layers of the inner shell. The whole inner shell may be manufactured by the currently available technique of magnetron sputtering, in which adjusting the W-Be concentration ratio can control the density gradient.

For the typical D^3S designs studied here, 1D LILAC simulations indicate that even with the current limit by CBET, a kinetic energy of ~ 30 to 40 kJ can still be coupled to the inner shell, which is about twice that of a typical indirect-drive double-shell target at a similar laser energy. If CBET is to be mitigated in the future, direct-drive double-shell targets should have even more margin. Nevertheless, the current CBET simulations can still give 1D neutron yields of ~ 6 MJ, roughly corresponding to an energy gain of $G \sim 3$. Two-dimensional, high-mode DRACO simulations have also been performed for these D^3S designs by including beam port geometry and laser imprint up to a maximum mode of $\ell = 150$. Since the implosion is in a very high adiabat ($\alpha \geqslant 10$), the outer Be shell is hardly affected by laser imprint.

Converging by only a factor of $\sim$3 and having a peak velocity of $\sim$240 km/s, the outer Be shell with good integrity impacts on the inner shell. This collision creates a high-pressure reservoir of $P > 2$ Gbar, which accelerates the inner shell to a final velocity of $\sim$230 km/s ($\sim$30 kJ kinetic energy). Because of the filtering of the CH-foam layer, only long-wavelength perturbations of the outer shell "imprint" onto the inner shell. However, these low-mode perturbations can exponentially grow during the deceleration phase, which has been found to be the main mechanism for reducing target performance in our current D^3S designs. Note that even the best laser overlapping ($R_{\text{beam}}/R_{\text{target}} = 0.85$–1.0) with OMEGA-type beam geometry can still give 0.5–1%(σ_{rms}) laser intensity perturbation with a dominant mode of $\ell = 10$. It is also noted that target shimming might be a way to compensate these long-wavelength laser perturbations. Regardless of these devastating perturbations, our DRACO simulations indicate that DT-plasma self-heating and burning can still occur, resulting in neutron yields of 300–1000 kJ. We argue that direct-drive double-shell implosions might provide a robust platform for burning-plasma physics studies. Optimizing these D^3S designs for polar-direct-drive (PDD) geometry [54] on the NIF, scaling them down to OMEGA size for experimental testing [55,56], and determining the acceptable specifications for target surface roughness will be topics of our future studies. Other important topics, such as the PDD geometry effect and the asphericity caused by the fact that the foam and outer shell will possibly be made from two hemispheres, will be further explored. Finally, we expect that once CBET is mitigated and/or more laser energy becomes available in the near future, direct-drive double-shell implosions may still be a viable way to reach ignition break even and a modest energy gain.

As history often told us, any uncertainty and less-understood physics in complex ICF designs can give over-optimistic results. The alternative D^3S can also have the possibility to suffer from the similar physics uncertainties as that of central hot-spot ignition designs. However, we expect that the D^3S implosions should be less sensitive to some of the physics uncertainties such as shock timing and adiabat control, although short-wavelength mixing needs a special care in D^3S target designs. In addition, the recent statistical-modeling and/or genetic-algorithm to design ICF targets [57,58] shall be able to help in optimizing D^3S implosion designs.

[1] J. Nuckolls, L. Wood, A. Thiessen, and G. Zimmerman, Nature (London) **239**, 139 (1972).

[2] C. Cherfils-Clérouin, C. Boniface, M. Bonnefille, P. Fremerye, D. Galmiche, P. Gauthier, J. Giorla, F. Lambert, S. Laffite, S. Liberatore, P. Loiseau, G. Malinie, L. Masse, P. E. Masson-Laborde, M. C. Monteil, F. Poggi, P. Seytor, F. Wagon, and J. L. Willien, J. Phys.: Conf. Ser. **244**, 022009 (2010).

[3] M. J. Edwards, J. D. Lindl, B. K. Spears, S. V. Weber, L. J. Atherton, D. L. Bleuel, D. K. Bradley, D. A. Callahan, C. J. Cerjan, D. Clark, G. W. Collins, J. E. Fair, R. J. Fortner, S. H. Glenzer, S. W. Haan, B. A. Hammel, A. V. Hamza, S. P. Hatchett, N. Izumi, and B. Jacoby *et al.*, Phys. Plasmas **18**, 051003 (2011).

[4] D. D. Meyerhofer, R. L. McCrory, R. Betti, T. R. Boehly, D. T. Casey, T. J. B. Collins, R. S. Craxton, J. A. Delettrez, D. H. Edgell, R. Epstein, K. A. Fletcher, J. A. Frenje, V. Yu. Glebov, V. N. Goncharov, D. R. Harding, S. X. Hu, I. V. Igumenshchev, J. P. Knauer, C. K. Li, and J. A. Marozas *et al.*, Nucl. Fusion **51**, 053010 (2011).

[5] R. S. Craxton, K. S. Anderson, T. R. Boehly, V. N. Goncharov, D. R. Harding, J. P. Knauer, R. L. McCrory, P. W. McKenty, D. D. Meyerhofer, J. F. Myatt, A. J. Schmitt, J. D. Sethian, R. W. Short, S. Skupsky, W. Theobald, W. L. Kruer, K. Tanaka,

R. Betti, T. J. B. Collins, and J. A. Delettrez *et al.*, Phys. Plasmas **22**, 110501 (2015).

[6] R. Betti and O. A. Hurricane, Nat. Phys. **12**, 435 (2016).

[7] D. S. Clark, A. L. Kritcher, S. A. Yi, A. B. Zylstra, S. W. Haan, and C. R. Weber, Phys. Plasma **25**, 032703 (2018); D. S. Clark, C. R. Weber, A. L. Kritcher, J. L. Milovich, P. K. Patel, S. W. Haan, B. A. Hammel, J. M. Koning, M. M. Marinak, M. V. Patel, C. R. Schroeder, S. M. Sepke, and M. J. Edwards, Nucl. Fusion **59**, 032008 (2018).

[8] I. V. Igumenshchev, V. N. Goncharov, W. T. Shmayda, D. R. Harding, T. C. Sangster, and D. D. Meyerhofer, Phys. Plasmas **20**, 082703 (2013).

[9] V. N. Goncharov, T. C. Sangster, R. Betti, T. R. Boehly, M. J. Bonino, T. J. B. Collins, R. S. Craxton, J. A. Delettrez, D. H. Edgell, R. Epstein, R. K. Follett, C. J. Forrest, D. H. Froula, V. Yu. Glebov, D. R. Harding, R. J. Henchen, S. X. Hu, I. V. Igumenshchev, R. Janezic, J. H. Kelly, and T. J. Kessler *et al.*, Phys. Plasmas **21**, 056315 (2014).

[10] S. X. Hu, D. T. Michel, A. K. Davis, R. Betti, P. B. Radha, E. M. Campbell, D. H. Froula, and C. Stoeckl, Phys. Plasmas **23**, 102701 (2016).

[11] D. T. Michel, S. X. Hu, A. K. Davis, V. Yu. Glebov, V. N. Goncharov, I. V. Igumenshchev, P. B. Radha, C. Stoeckl, and D. H. Froula, Phys. Rev. E **95**, 051202(R) (2017).

[12] S. E. Bodner, Phys. Rev. Lett. **33**, 761 (1974).

[13] H. Takabe, K. Mima, L. Montierth, and R. L. Morse, Phys. Fluids **28**, 3676 (1985).

[14] N. Metzler, A. L. Velikovich, and J. H. Gardner, Phys. Plasmas **6**, 3283 (1999).

[15] A. Casner, D. Galmiche, and G. Huser, Phys. Plasmas **16**, 092701 (2009).

[16] V. A. Smalyuk, S. X. Hu, J. D. Hager, J. A. Delettrez, D. D. Meyerhofer, T. C. Sangster, and D. Shvarts, Phys. Rev. Lett. **103**, 105001 (2009).

[17] A. Casner, C. Mailliet, and G. Rigon, Nuclear Fusion **59**, 032002 (2019).

[18] T. R. Boehly, D. H. Munro, P. M. Celliers, R. E. Olson, D. G. Hicks, V. N. Goncharov, G. W. Collins, H. F. Robey, S. X. Hu, J. A. Marozas, T. C. Sangster, O. L. Landen, and D. D. Meyerhofer, Phys. Plasmas **16**, 056302 (2009).

[19] T. R. Boehly, V. N. Goncharov, W. Seka, S. X. Hu, J. A. Marozas, D. D. Meyerhofer, P. M. Celliers, D. G. Hicks, M. A. Barrios, D. Fratanduono, and G. W. Collins, Phys. Plasmas **18**, 092706 (2011); T. R. Boehly, V. N. Goncharov, W. Seka, M. A. Barrios, P. M. Celliers, D. G. Hicks, G. W. Collins, S. X. Hu, J. A. Marozas, and D. D. Meyerhofer, Phys. Rev. Lett. **106**, 195005 (2011).

[20] H. F. Robey, T. R. Boehly, P. M. Celliers, J. H. Eggert, D. Hicks, R. F. Smith, R. Collins, M. W. Bowers, K. G. Krauter, P. S. Datte, D. H. Munro, J. L. Milovich, O. S. Jones, P. A. Michel, C. A. Thomas, R. E. Olson, S. Pollaine, R. P. J. Town, S. Haan, and D. Callahan *et al.*, Phys. Plasmas **19**, 042706 (2012).

[21] D. T. Michel, A. V. Maximov, R. W. Short, S. X. Hu, J. F. Myatt, W. Seka, A. A. Solodov, B. Yaakobi, and D. H. Froula, Phys. Rev. Lett. **109**, 155007 (2012).

[22] M. J. Rosenberg, A. A. Solodov, J. F. Myatt, W. Seka, P. Michel, M. Hohenberger, R. W. Short, R. Epstein, S. P. Regan, E. M. Campbell, T. Chapman, C. Goyon, J. E. Ralph, M. A. Barrios, J. D. Moody, and J. W. Bates, Phys. Rev. Lett. **120**, 055001 (2018).

[23] M. Tabak, J. Hammer, M. E. Glinsky, W. L. Kruer, S. C. Wilks, J. Woodworth, E. M. Campbell, M. D. Perry, and R. J. Mason, Phys. Plasmas **1**, 1626 (1994).

[24] P. A. Norreys, R. H. H. Scott, and K.L. Lancaster, Nucl. Fusion **49**, 104023 (2009).

[25] R. Betti, C. D. Zhou, K. S. Anderson, J. L. Perkins, W. Theobald, and A. A. Solodov, Phys. Rev. Lett. **98**, 155001 (2007); W. Theobald, R. Nora, M. Lafon, A. Casner, X. Ribeyre, K. S. Anderson, R. Betti, J. A. Delettrez, J. A. Frenje, V. Yu. Glebov, O. V. Gotchev, M. Hohenberger, S. X. Hu, F. J. Marshall, D. D. Meyerhofer, T. C. Sangster, G. Schurtz, W. Seka, V. A. Smalyuk, C. Stoeckl, and B. Yaakobi, Phys. Plasmas **19**, 102706 (2012).

[26] W. S. Varnum, N. D. Delamater, S. C. Evans, P. L. Gobby, J. E. Moore, J. M. Wallace, R. G. Watt, J. D. Colvin, R. Turner, V. Glebov, J. Soures, and C. Stoeckl, Phys. Rev. Lett. **84**, 5153 (2000).

[27] P. Amendt, J. D. Colvin, R. E. Tipton, D. E. Hinkel, M. J. Edwards, O. L. Landen, J. D. Ramshaw, L. J. Suter, W. S. Varnum, and R. G. Watt, Phys. Plasmas **9**, 2221 (2002).

[28] J. Milovich, P. Amendt, M. Marinak, and H. Robey, Phys. Plasmas **11**, 1552 (2004).

[29] P. A. Amendt, H. F. Robey, H.-S. Park, R. E. R. E. Tipton, R. E. Turner, J. L. Milovich, M. Bono, R. Hibbard, H Louis,

R. Wallace, and V. Yu. Glebov, Phys. Rev. Lett. **94**, 065004 (2005).

[30] H. F. Robey, P. A. Amendt, J. L. Milovich, H.-S. Park, A. V. Hamza, and M. J. Bono, Phys. Rev. Lett. **103**, 145003 (2009).

[31] D. S. Montgomery, W. S. Daughton, B. J. Albright, A. N. Simakov, D. C. Wilson, E. S. Dodd, R. C. Kirkpatrick, R. G. Watt, M. A. Gunderson, E. N. Loomis, E. C. Merritt, T. Cardenas, P. Amendt, J. L. Milovich, H. F. Robey, R. E. Tipton, and M. D. Rosen, Phys. Plasmas **25**, 092706 (2018).

[32] K. Molvig, M. J. Schmitt, B. J. Albright, E. S. Dodd, N. M. Hoffman, G. H. McCall, and S.D. Ramsey, Phys. Rev. Lett. **116**, 255003 (2016).

[33] E. M. Campbell and W. J. Hogan, Plasma Phys. Control. Fusion **41**, B39 (1999).

[34] C. J. Randall, J. J. Thomson, and K. G. Estabrook, Phys. Rev. Lett. **43**, 924 (1979).

[35] I. V. Igumenshchev, D. H. Edgell, V. N. Goncharov, J. A. Delettrez, A. V. Maximov, J. F. Myatt, W. Seka, A. Shvydky, S. Skupsky, and C. Stoeckl, Phys. Plasmas **17**, 122708 (2010).

[36] D. H. Froula, T. J. Kessler, I. V. Igumenshchev, R. Betti, V. N. Goncharov, H. Huang, S. X. Hu, E. Hill, J. H. Kelly, D. D. Meyerhofer, A. Shvydky, and J. D. Zuegel, Phys. Plasmas **20**, 082704 (2013).

[37] J. A. Marozas, M. Hohenberger, M. J. Rosenberg, D. Turnbull, T. J. B. Collins, P. B. Radha, P. W. McKenty, J. D. Zuegel, F. J. Marshall, S. P. Regan, T. C. Sangster, W. Seka, E. M. Campbell, V. N. Goncharov, M. W. Bowers, J.-M. G. Di Nicola, G. Erbert, B. J. MacGowan, L. J. Pelz, J. D. Moody, and S. T. Yang, Phys. Plasmas **25**, 056314 (2018).

[38] H. Xu, H. Huang, J. Walker, C. Kong, N. G. Rice, M. P. Mauldin, J. D. Vocke, J. H. Bae, W. Sweet, F. H. Elsner, M. P. Farrell, Y. M. Wang, C. Alford, T. Cardenas, and E. Loomis, Fusion Sci. Technol. **73**, 354 (2018).

[39] J. D. Lindl, P. Amendt, R. L. Berger, S. G. Glendinning, S. H. Glenzer, S. W. Haan, R. L. Kauffman, O. L. Landen, and L. J. Suter, Phys. Plasmas **11**, 339 (2004).

[40] J. Delettrez, R. Epstein, M. C. Richardson, P. A. Jaanimagi, and B. L. Henke, Phys. Rev. A **36**, 3926 (1987).

[41] P. B. Radha, T. J. B. Collins, J. A. Delettrez, Y. Elbaz, R. Epstein, V. Yu. Glebov, V. N. Goncharov, R. L. Keck, J. P. Knauer, J. A. Marozas, F. J. Marshall, R. L. McCrory, P. W. McKenty, D. D. Meyerhofer, S. P. Regan, T. C. Sangster, W. Seka, D. Shvarts, S. Skupsky, Y. Srebro, and C. Stoeckl, Phys. Plasmas **12**, 056307 (2005).

[42] G. P. Schurtz, Ph. D. Nicolaï, and M. Busquet, Phys. Plasmas **7**, 4238 (2000).

[43] D. Cao, G. Moses, and J. Delettrez, Phys. Plasmas **22**, 082308 (2015).

[44] S. X. Hu, B. Militzer, V. N. Goncharov, and S. Skupsky, Phys. Rev. Lett. **104**, 235003 (2010).

[45] S. X. Hu, B. Militzer, V. N. Goncharov, and S. Skupsky, Phys. Rev. B **84**, 224109 (2011).

[46] S. X. Hu, T. R. Boehly, and L. A. Collins, Phys. Rev. E **89**, 063104 (2014); S. X. Hu, L. A. Collins, V. N. Goncharov, J. D. Kress, R. L. McCrory, and S. Skupsky, *ibid.* **92**, 043104 (2015).

[47] Y. H. Ding and S. X. Hu, Phys. Plasmas **24**, 062702 (2017).

[48] S. X. Hu, L. A. Collins, V. N. Goncharov, T. R. Boehly, R. Epstein, R. L. McCrory, and S. Skupsky, Phys. Rev. E **90**, 033111 (2014).

[49] S. X. Hu, L. A. Collins, J. P. Colgan, V. N. Goncharov, and D. P. Kilcrease, Phys. Rev. B **96**, 144203 (2017).

[50] R. Epstein, T. J. B. Collins, J. A. Delettrez, S. Skupsky, and R. P. J. Town, Bull. Am. Phys. Soc. **43**, 1666 (1998).

[51] D. T. Michel, V. N. Goncharov, I. V. Igumenshchev, R. Epstein, and D. H. Froula, Phys. Rev. Lett. **111**, 245005 (2013).

[52] S. X. Hu, V. N. Goncharov, P. B. Radha, J. A. Marozas, S. Skupsky, T. R. Boehly, T. C. Sangster, D. D. Meyerhofe, and R. L. McCrory, Phys. Plasmas **17**, 102706 (2010).

[53] K. Molvig, M. J. Schmitt, R. Betti, E. M. Campbell, and P. McKenty, Phys. Plasmas **25**, 082708 (2018).

[54] S. Skupsky, J. A. Marozas, R. S. Craxton, R. Betti, T. J. B. Collins, J. A. Delettrez, V. N. Goncharov, P. W. McKenty, P. B. Radha, T. R. Boehly, J. P. Knauer, F. J. Marshall, D. R. Harding, J. D. Kilkenny, D. D. Meyerhofer, T. C. Sangster, and R. L. McCrory, Phys. Plasmas **11**, 2763 (2004).

[55] G. A. Kyrala, M. A. Gunderson, N. D. Delamater, D. A. Haynes, D. C. Wilson, J. A. Guzik, and K. A. Klare, Phys. Plasmas **13**, 056306 (2006.

[56] B. S. Scheiner, M. J. Schmitt, S. C. Hsu, D. Schmidt, J. Mance, C. Wilde, D. N. Polsin, T. R. Boehly, F. J. Marshall, N. Krasheninnikova, K. Molvig, and H. Huang, Phys. Plasmas **26**, 072707 (2019).

[57] V. Gopalaswamy *et al.*, Nature (London) **565**, 581 (2019).

[58] P. W. Hatfield, S. J. Rose, and R. H. H. Scott, Phys. Plasmas **26**, 062706 (2019).